XMM-Newton CCF Release Note

XMM-CAL-SRN-0313

Refinement of the high-energy XRT3 PSF

Matteo Guainazzi, Pedro Rodriguez-Pascual, Richard Saxton, Martin Stuhlinger

18 March 2014

1 CCF components

Name of CCF	VALDATE	EVALDATE	Blocks changed	XSCS flag
XRT3_XPSF_0016.CCF	2001-01-13		ELLBETA	No

We present a refinement of the high-energy ($E \geq 2$ keV) on-axis Point Spread Function (PSF) of the XMM-Newton XRT3 telescope, on whose focus the EPIC-pn camera (Aschenbach et al., 2000) is located. This update aims at fixing an issue unveiled with SASv13 (cf. Fig. 1): the high-energy fluxes measured on a point-like source (Mkn 421, Obs.#0153951201 in Fig. 1) in en EPIC-pn Timing Mode exposure. as a function of the number of excised columns around the boresight were discovered to be less stable when the effective area was calculated with the default `ELLBETA` rather than with the `EXTENDED` PSF model.

The condition that the measured fluxes shall be invariant with respect to the number of excised columns can be used to optimise the parameters describing the XRT3 PSF wings. This idea underpins the CCF change described in this Release Note (RN).

2 Changes

In Fig. 2 we show the on-axis parameters of `XRT3_PSF_0014.CCF` as a function of energy (Read et al. 2011). The changes introduced with this version can be summarised as follows:

1. the r_0 and α values at 10.25 keV and 15 keV were replaced with their linear extrapolation at lower energies. The goal of this change is avoiding large gradients in the energy dependence of these parameters. This change affects the Encircled Energy Fraction (EEF) calculation only above 10 keV. It is therefore negligible for any practical analysis in the imaging or spectral domain

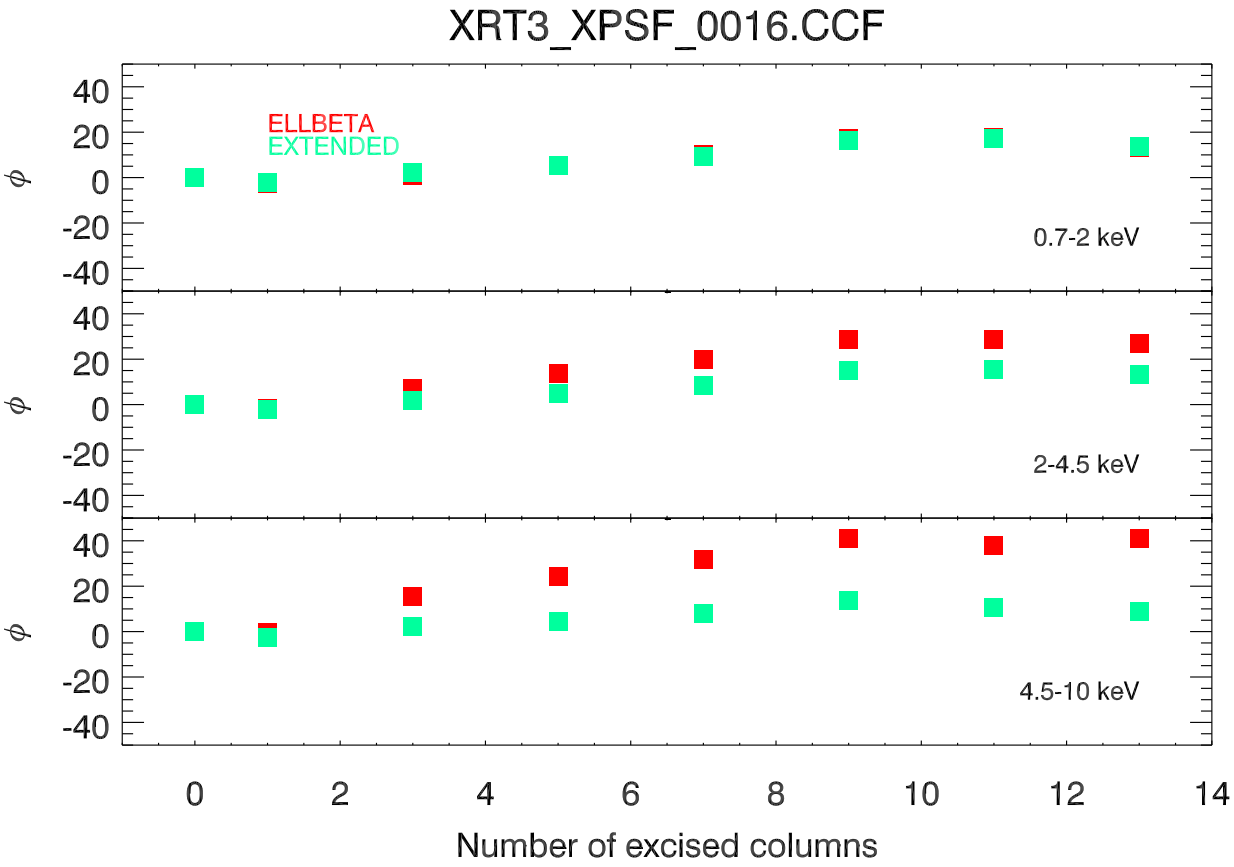

Figure 1: Percentage difference of the flux measured on the XRT3 PSF wings as a function of the number of excised columns around the boresight. The quantity on the y-axis is defined as $\phi(x) \equiv 100.0 \times \frac{F_0 - F_x}{F_0}$, where F_0 is the flux extracted from the whole PSF (extraction radius equal to 15 pixels in `RAWX`), and F_x is the flux measured after excising x columns around the boresight. The three panels correspond to the soft (0.7-2 keV; *top*), intermediate (2–4.5 keV; *middle*), and hard (4.5–10 keV; *bottom*) energy bands. The *green* data points correspond to the `EXTENDED`, the *red* data points to the `ELLBETA` PSF model.

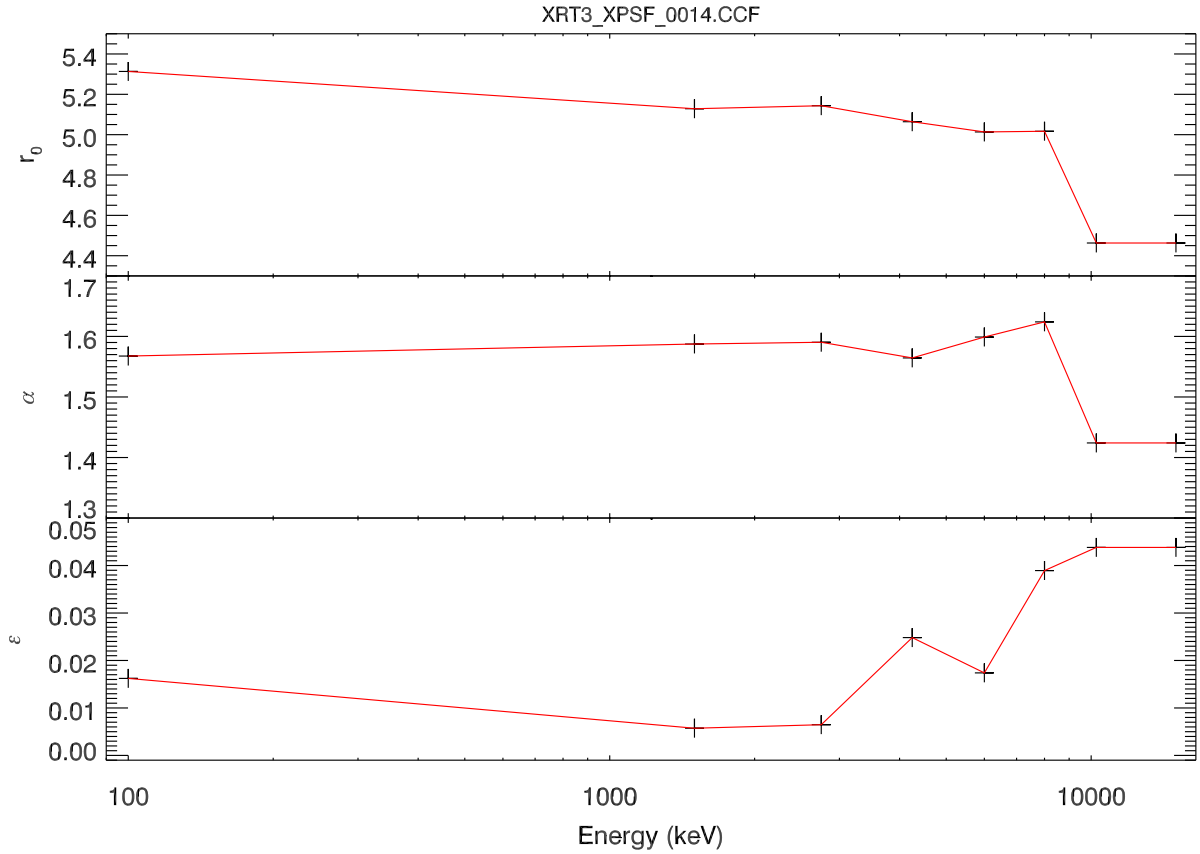

Figure 2: On-axis ELLBETA parameters as a function of energy in XRT3_PSF_0014.CCF

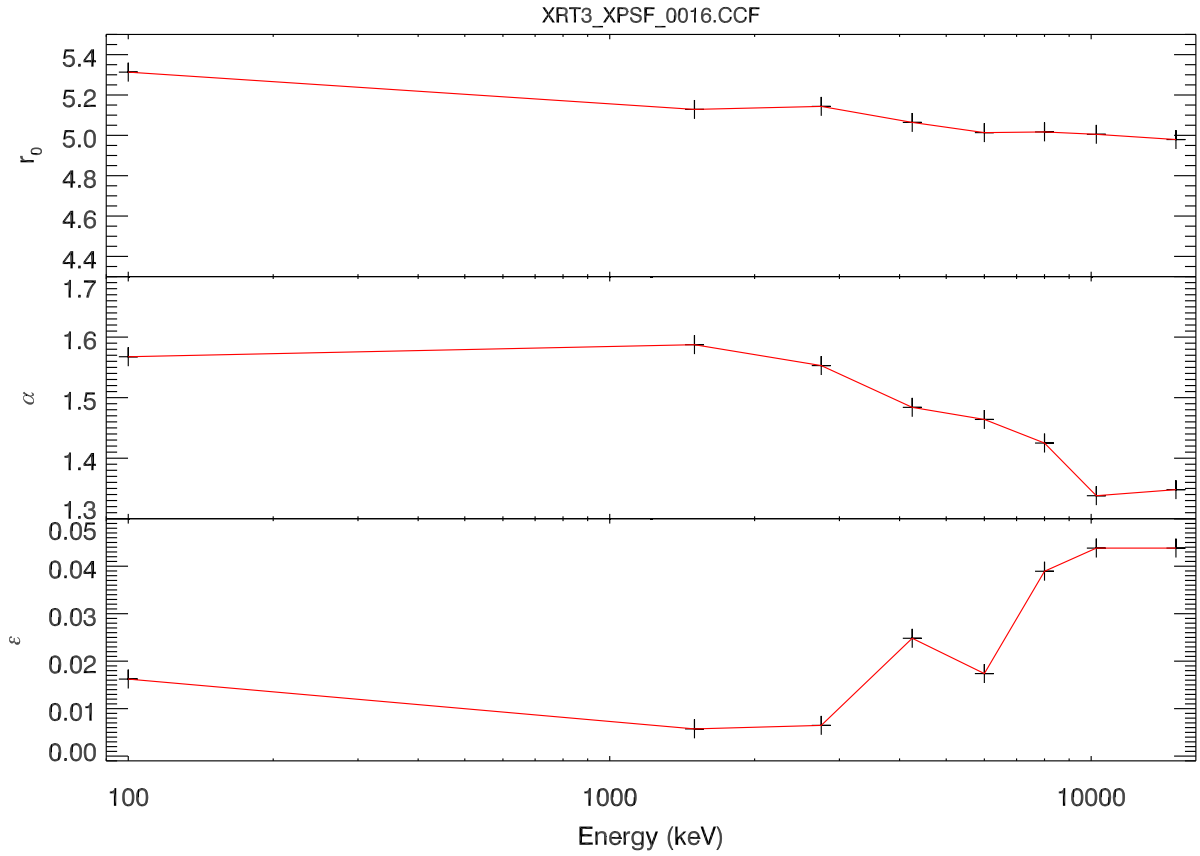

Figure 3: The same as Fig. 2 for `XRT3_PSF_0016.CCF`

2. test XRT3 PSF files were generated by varying the r_0 and α energy-dependence above 2 keV according to linear function equal to 0 at 2 keV and η_i at 10.5 keV, with η_i comprised in the $\pm$30% range in steps of 2%, and i equal to either r_0 or α

The dependency of the flux as a function of the number of excised columns around the boresight was studied for each test PSF generated in Step#2 above. We used the parameter $\phi(x)$, defined as $100.0 \times \frac{F_0 - F_x}{F_0}$, where F_0 is the flux extracted from the whole PSF (extraction radius equal to 15 pixels in `RAWX`), and F_x is the flux measured after excising x columns around the boresight. The change embedded in `XRT3_PSF_0016.CCF` corresponds to η_α = -16%, the value minimising the average $\phi(x)$. The new XRT3 PSF parameters as a function of energy are shown in Fig. 3.

3 Scientific Impact of this Update

The goal of this update is improving the stability of the high-energy fluxes measured from the wing of the PSF, without compromising the accuracy of the source detection. As shown in Sect. 5.1, the updated `ELLBETA` parametrisation improves the EEF stabil-

ity with respect to the EXTENDED model above 4.5 keV, while yielding indistinguishable performances at lower energies. The impact on the source detection is also negligible (cf. Sect. 5.3).

4 Estimated Scientific Quality

The main goal of this PSF update is achieving a stability of the high-energy EEF calculation in the XRT3 PSF wings within ±5%. As shown in Sect. 5.1, this goal is achieved for the hardest energy range (E≥4.5 keV) only. Larger uncertainties at lower energies (now independent of the PSF model being used) are under investigation.

5 Test procedures and results

5.1 Spectral domain: EPIC-pn Timing Mode

Fig. 4 shows the measured fluxes (normalised to the whole PSF flux) as a function of the number of excised columns for the same observation as in Fig. 1 when the effective areas are calculated using XRT3_PSF_0016.CCF. In the hardest energy range (E≥4.5 keV) the EEF is stable within a few percent. At lower energies, instabilities are still present, reaching up to ≃15% in the farthest wings. However, with XRT3_PSF_0016.CCF the EEF calculations based on the ELLBETA model are consistent with those based on the EXTENDED model. This might indicate that residuals EEF calculation instabilities are primarily driven by SAS issues.

5.2 Spectral domain: EPIC-pn imaging mode

Fig. 5 shows the stacked residuals on a sample of 45 Radio-Loud AGN (primarily blazars) observed by EPIC-pn in imaging modes, mostly Small Window. The stacked residual technique follows the algorithm described in Longinotti et al. (2008), and Kettula et al. (2013), assuming that each individual spectrum is well described by a photoelectrically absorbed logarithmically curved power-law. Spectra, whose best-fit corresponds to a reduced χ^2 higher than 1.5, were not included in the stacked residuals spectrum. The RLAGN sample sources are affected by pile-up, and their spectra are therefore extracted after excising the PSF core up to achieving a pile-up free annulus (see Stuhlinger et al. 2010 for a detailed description of the spectral reduction). The outer radius of the spectra accumulation annuli were chosen to ptimize the signal-to-noise ratio. Below ≃2 keV the stacked residuals spectra obtained with the XRT3_PSF_0014.CCF (*red points* in Fig. 5) and the XRT3_PSF_0016.CCF (*black points*) ELLBETA PSF models are consistent within the statistical uncertainties (shown at the 1σ level as the error on the mean value for each stacked residuals channel). However, the residuals obtained with XRT3_PSF_0014.CCF

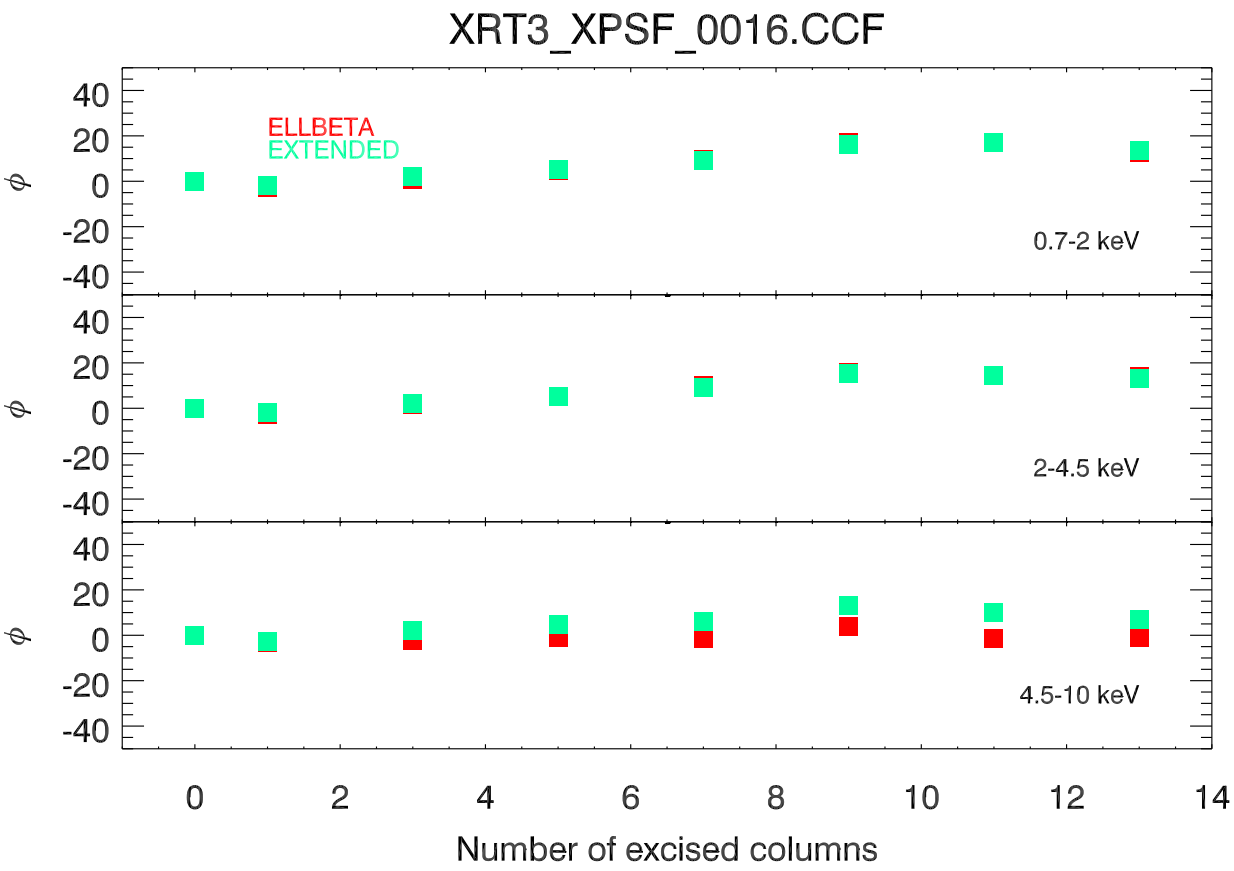

Figure 4: The same as Fig. 1 when the effective areas are calculated using `XRT3_PSF_0016.CCF`.

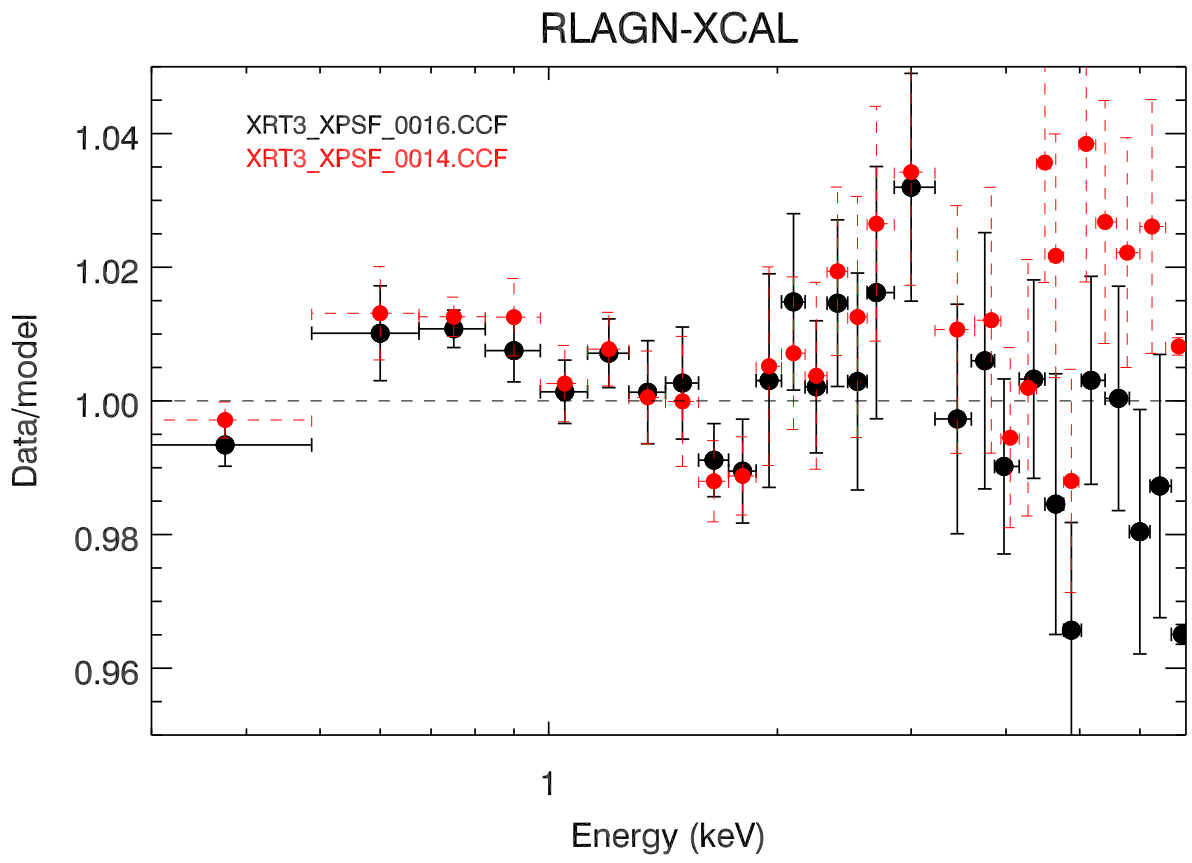

Figure 5: Stacked residuals against their best-fit logarithmic power-law model for a sample of RLAGN, whose spectra are extracted from annuli around the PSF centroid to avoid pile-up. The *red points* correspond to EEF calculated using `XRT3_PSF_0014.CCF`, the *black points* to that calculated using `XRT3_PSF_0016.CCF`.

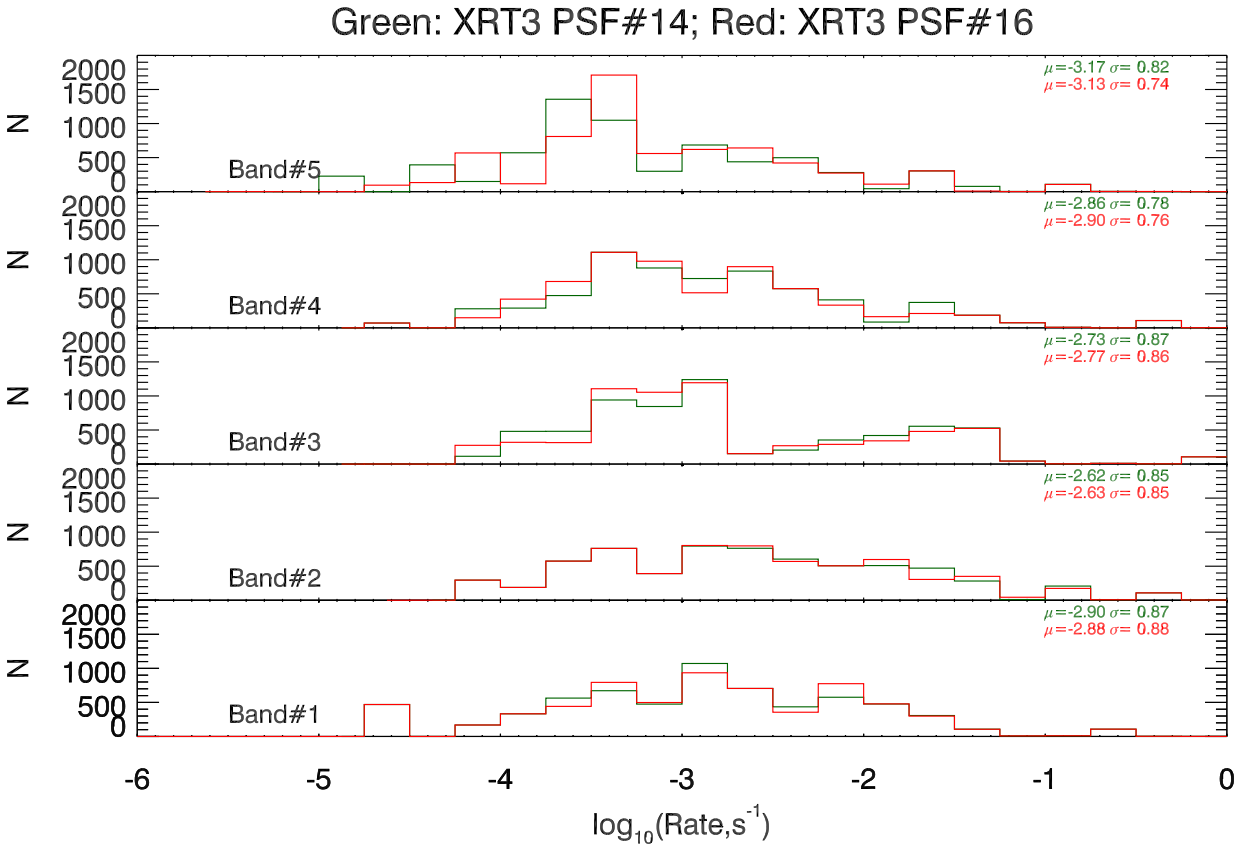

Figure 6: Distribution of count rates in the five 3XMM energy bands when the final step of source detection in the XMM-Newton data processing pipeline is performed with `XRT3_PSF_0014.CCF` (*green*) and `XRT3_PSF_0016.CCF` (*red*). The numbers in each panel represent the mean and standard deviation of the distributions.

above 2 keV exhibit an excess by $\simeq$2%. This excess disappears when the EEF is calculated using `XRT3_PSF_0016.CCF`. This is a further evidence in favour of the new CCF representing a more accurate calibration of the high-energy PSF wings.

5.3 Spatial domain: EPIC-pn imaging mode

The `XRT3_PSF_0016.CCF` was used for the last stage of the source detection in the XMM-Newton processing pipeline (on which the generation of the EPIC serendipitous source catalogue is based: Watson et al. 2009) on a random sample of 150 recent observations. Its performances are compared in Fig. 6 against `XRT3_PSF_0014.CCF` in terms of detected count rate per energy band. The difference on the averages of the count rate distributions is <0.05 dex even for the hardest energy band. The fraction of mis-matched sources (*i.e.* source detected with one PSF model, and undetected with the other) is 0.12% out of about 6,500 sources.

6 Expected updates

The method outlined in this RN could in principle be used to achieve further improvements in the stability of the EEF calculated in the PSF wings. It could be extended also to the optics focusing onto the EPIC-MOS cameras.

References

Aschenbach B., et al., 2000, SPIE, 4012, 731

Kettula K., et al., 2013, A&A, 552, 47

Longinotti A., et al., 2008, RMxAC, 32, 62

Read A.M., et al., 2011, A&A, 534, 34

Stuhlinger et al., 2010, XMM-SOC-CAL-TN-0051, (available at:
`http://xmm2.esac.esa.int/docs/documents/CAL-TN-0052.ps.gz`)

Watson M., et al., 2009, A&A, 493, 339